

# QoS Aware Robot Trajectory Optimization with IRS-Assisted Millimeter-Wave Communications

Cristian Tatino, *Student Member, IEEE*, Nikolaos Pappas, *Member, IEEE*,  
and Di Yuan, *Senior Member, IEEE*

## Abstract

This paper considers the motion energy minimization problem for a wirelessly connected robot using millimeter-wave (mm-wave) communications. These are assisted by an intelligent reflective surface (IRS) that enhances the coverage at such high frequencies characterized by high blockage sensitivity. The robot is subject to time and uplink communication quality of service (QoS) constraints. This is a fundamental problem in fully automated factories that characterize Industry 4.0, where robots may have to perform tasks with given deadlines while maximizing the battery autonomy and communication efficiency. To account for the mutual dependence between robot position and communication QoS, we propose a joint optimization of robot trajectory and beamforming at the IRS and access point (AP). We present a solution that first exploits mm-wave channel characteristics to decouple beamforming and trajectory optimization. Then, the latter is solved by a successive-convex optimization-based algorithm. The algorithm takes into account the obstacles' positions and a radio map to avoid collisions and poorly covered areas. We prove that the algorithm can converge to a solution satisfying the Karush-Kuhn-Tucker (KKT) conditions. The simulation results show a dramatic reduction of the motion energy consumption with respect to methods that aim to find maximum-rate trajectories. Moreover, we show how the IRS and the beamforming optimization improve the motion energy efficiency of the robot.

## Index Terms

Energy efficient motion, intelligent reflective surface, millimeter-waves, robot path planning.

This work was supported in part by CENIIT, ELLIIT, and by the European Union's Horizon 2020 research and innovation programme under the Marie Skłodowska-Curie grant agreement No. 643002 (ACT5G).

Cristian Tatino, Nikolaos Pappas, and Di Yuan are with Department of Science and Technology (ITN), Linköping University, Sweden (Email: cristian.tatino@liu.se, nikolaos.pappas@liu.se, di.yuan@liu.se)

## I. INTRODUCTION

Robotic and wireless technologies are playing a crucial role in Industry 4.0 leading to full automation of manufacturing processes, warehousing, and logistics [1]. However, an increasing number of robots and the rising of new industrial applications, with stringent quality of service (QoS) requirements, will toughly test the performance of the next generation of mobile communications, i.e., 6G. Specifically, real-time industrial applications such as augmented and virtual reality for assisted manufacturing or mining, may require Gbps for peak data rates [2]. Moreover, swarms consisting of hundreds of sensing robots in the warehouses of the future may need to be simultaneously connected and collaborate, with latency and reliability requirements of 1 ms and up to 99.9999%, respectively [2], [3].

Millimeter-wave (mm-wave) communications can provide a huge amount of bandwidth and throughput for satisfying data rate requirements for industrial applications [4]. However, high blockage sensitivity reduces communication reliability while robots move in environments with obstacles. These must be avoided by the robot, of which the trajectory highly affects mm-wave performance as it determines whether the robot is in line-of-sight (LOS) or non-line-of-sight (NLOS). Moreover, robots are battery limited and have tasks that are usually characterized by stringent deadlines. When a robot is out of energy, its battery must be charged with a cost of time and power. The latter can represent approximately 8% of the total electrical energy consumption for manufacturing processes [5]. Thus, optimized trajectories can reduce energy consumption and avoid poorly covered areas.

Besides trajectory optimization, several solutions have been proposed to enhance coverage in mm-waves scenarios, e.g., relays [6] and intelligent reflective surfaces (IRSs) [7]–[9]. The latter consist of arrays of reflective elements that can be electronically controlled to adjust the angle and the phase of the reflected signals to be either added coherently or destructively to the receiver [10], [11]. Moreover, due to the small wavelength, IRSs with many reflective elements can be deployed at mm-waves with a lower cost and negligible energy consumption than active relays to provide alternative paths to the direct link in case of blockages [12]. These characteristics make IRSs ideal candidates for enhancing throughput, reliability, and energy efficiency of robot communications at high frequencies. However, beamforming at the IRS must be set according to the channel that depends on the robot trajectory. Hence, in this work, we consider wirelessly connected robots in IRS-assisted mm-wave scenarios, where trajectory and beamforming are

optimized to minimize the motion energy consumption. To solve this problem, we propose a modified successive convex optimization (SCO) algorithm that accounts for the knowledge of the environment and a radio map to avoid collisions and satisfy time and QoS constraints.

#### A. Related Works

Energy minimization has been one of the most important problems in robot trajectory optimization [13]–[17]. In [13], the authors model the power consumption of a DC motor-equipped robot as a function of the speed, and they show up to 50% of energy-saving when an optimal control of the robot’s speed is performed. The work in [14] considers a graph-based method and A\* algorithm to determine the minimum cost path of a robot, where the cost of an edge is computed according to the motion energy consumption. A convex optimization approach is used in [15], which presents an alternating quadratic programming method to determine the path that minimizes the energy consumption in scenarios with obstacles. Multi-robot scenarios are considered by [16], where the authors solve the problem of minimizing the time for completing tasks and energy consumption.

Wirelessly connected robots are considered in [17]. This work proposes a joint robot communication and motion energy minimization by controlling transmit power and robot’s speed along a fixed trajectory. More precisely, the possibility to control the robot motion introduces a new degree of freedom for resource allocation problems in wireless communications. In the past few years, several studies have explored this topic [18]–[24]. Similar to [17], the work [18] considers an optimal control problem for motion and communication energy minimization subject to a certain amount of data to be transmitted. In this case, multiple robots are connected to an access point (AP). In [19], multiple robots must periodically perform surveillance tasks with the goal of maintaining connectivity with an AP by possibly exploiting multi-hop connectivity. Multi-hop connectivity for surveillance tasks are also considered in [20], where the robot need to periodically transmit data through an ad hoc network. Task optimizations in ad hoc wireless networks for multi-robot coordinations and transmissions are also taken into account by [21]–[24], where [24] considers directional communication scenarios.

Directional communications are typical of mm-wave communications that have recently attracted the interest of industrial applications [4], [25]–[27]. However, the potentials of mm-waves transmissions for wirelessly connected robots need to be further explored, even though some studies have been performed for unmanned aerial vehicle (UAV) scenarios [28], [29].

Mm-wave connected robots are considered in [30], where the authors present several instances of an association and path planning problem in multi-APs mm-wave wireless networks, where a graph-based algorithm is used to minimize handovers and travel time of multiple robots. A radio map is used to account obstacles and blockages that challenge mm-wave communications. Graph-based methods and radio maps are also used in [31] to optimize UAVs flying time distance while ensuring a target QoS requirement.

Several joint communication and trajectory planning problems have been proposed for UAV scenarios [32]–[36]. In [37]–[40], IRSs are used to enhance UAV-user communications, and [39], [40] perform a joint trajectory and beamforming optimization to maximize the received power at the users. However, especially in mm-wave scenarios, UAV communications do not present the same characteristics of wirelessly connected robots.

### B. Contributions

The contributions of this paper are summarized as follows:

- We consider a novel trajectory optimization problem for robots with IRS-assisted mm-wave communications. The problem aims to minimize the motion energy consumption while satisfying minimum average data rate and time constraints, and avoiding collisions with obstacles. To the best of our knowledge, energy-efficient trajectory planning problems for wirelessly connected robots have not been considered for mm-wave communications that face particular signal propagation conditions. Moreover, we consider the impact of joint trajectory and the beamforming optimization on the energy consumption and achieved data rate. Joint IRS beamforming and trajectory optimization has been analyzed only for maximizing the data rate in UAV scenarios; however, robot trajectories must account for obstacle avoidance and more severe NLOS conditions.
- We propose a SCO-based algorithm (*RMAP*) that deals with non-convexity of the data rate as a function of the robot position in mm-wave scenarios when obstacles create abrupt LOS-NLOS transitions. Specifically, we use a radio map to establish if a trajectory solution satisfies the QoS constraint. Radio map information can easily be included in graph-based methods. However, these methods may poorly perform when applied to our problem due to the average data rate constraint.
- We prove that the proposed SCO algorithm converges and, under certain conditions, it converges to a point satisfying KKT conditions of the problem. The proposed method can

find trajectories that avoid collisions and satisfy the QoS requirement by using the radio map information. Moreover, we show how the algorithm can reduce dramatically the energy consumption with respect to trajectories that maximize the data rate. Finally, we show how IRSs can enhance the motion energy efficiency for QoS constrained wirelessly connected robot.

The rest of the paper is organized as follows. In Section II we describe the system model. In Section III, we formulate the problem and exploit mm-wave propagation characteristics to decouple beamforming and trajectory optimizations. In Section IV, we solve the latter by using a SCO algorithm, and in Section V, we provide performance evaluation. Finally, Section VI concludes the paper.

## II. SYSTEM MODEL AND ASSUMPTIONS

We consider an industrial scenario, e.g., an industrial plant, where a robot moves from a starting position  $q_s$  to its goal  $q_d$  within a time horizon of fixed duration. The robot moves on the horizontal plane of a 3D restricted area characterized by the presence of several 3D obstacles. These are represented by a set  $\mathcal{O}$  of cylinders with elliptic bases and given heights.<sup>1</sup> The area is covered by an AP using mm-waves to which the robot needs to transmit uplink data by maintaining a certain communication QoS. This is expressed as a minimum average data rate requirement ( $r_{min}$ ). The robot is equipped with a single antenna, whereas, the AP is equipped with a uniform linear array (ULA) with  $N$  antennas. The robot-AP communication is assisted by an IRS consisting of  $M$  reflective elements, of which the phase shifters are adjusted by a controller, which shares the channel state information (CSI) with the AP. A scheduler, which we assume to be co-located with the controller, optimizes the robot trajectory and the beamforming to minimize the motion energy consumption. We consider both active and passive beamforming at the AP and IRS, respectively.

*Notations:*  $(.)^T$  and  $(.)^H$ , represents the transpose and the conjugate transpose, respectively;  $diag(.)$  returns the diagonalization of a vector and  $arg(.)$  denotes the phase of a complex number. Finally,  $\|.\|_n$  represents the  $n$ -norm. Moreover, a summary of the notation is available in Table I.

<sup>1</sup>Note that an arbitrarily shaped obstacle can be approximated by the intersection and the union of several convex shapes [41]. In this paper, we consider 3D cylinders with elliptic bases, but this work can be generalized to the choice of other convex shapes.

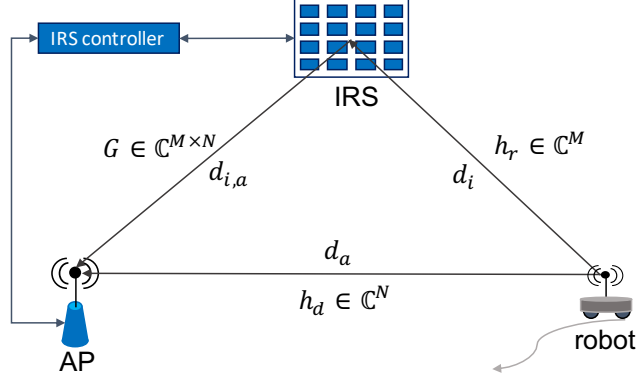


Fig. 1: A scenario consisting of an IRS-aided robot uplink communication.

### A. Robot Motion Model

The robot must avoid collisions with obstacles and reach the destination within a given deadline. We divide the time horizon in  $K$  timeslots,  $k = 0, \dots, K$ , of duration  $\Delta_t$ . In each timeslot, we assume that the location of the robot and channel conditions do not change. Moreover, within a timeslot, the robot can travel for a maximum distance of  $D_{max} = v_{max}\Delta_t$ , where,  $v_{max}$  is the maximum speed. A trajectory of the robot can be represented as a sequence  $\mathbf{q} = [q_0, q_1, \dots, q_K]$ , where  $q_0 = q_s$  and  $q_K = q_d$ . The term  $q_k = [x_k, y_k]$ ,  $k = 0, \dots, K$ , represents the Cartesian coordinates of the robot on the horizontal plane in the  $k$ -th timeslot. Let  $q_a = [x_a, y_a]$  and  $q_i = [x_i, y_i]$  represents the fixed positions of the AP and the IRS, respectively. The altitude of the robot is fixed at its antenna height  $z_r$ , whereas  $z_a$  represents the height at which the AP is installed and  $z_i$  the height of the IRS.

Let  $v_k$  be the speed of the robot at the  $k$ -th timeslot. Then, the motion energy consumption of the DC motor-equipped robot along the path can be written as follows [17]:

$$\begin{aligned}
 E &= \sum_{k=1}^{K} E_k = \sum_{k=1}^{K} c_1 v_k^2 \Delta_t + c_2 v_k \Delta_t + c_3 \Delta_t = \\
 &\sum_{k=1}^{K} c_1 \frac{\|q_k - q_{k-1}\|_2^2}{\Delta_t} + c_2 \|q_k - q_{k-1}\|_2 + c_3 \Delta_t,
 \end{aligned} \tag{1}$$

where,  $E_k$  is the energy consumption in the  $k$ -th timeslot, and  $c_1$ ,  $c_2$ , and  $c_3$  are positive constants depending on the characteristics of the robot and external load.

### B. Channel Model

As shown in Fig. 1, let  $h_r \in \mathbb{C}^M$  be the channel vector between the robot and the IRS and  $G \in \mathbb{C}^{M \times N}$  denote the channel matrix between the IRS and the AP. The direct channel between the robot and the AP is represented by vector  $h_d \in \mathbb{C}^M$ . Then, the received baseband signal at the AP at timeslot  $k$  can be written as follows:

$$y_k = (h_{r,k}^H \Phi_k G_k + h_{d,k}^H) w_k \sqrt{p_t} s_k + \eta_k, \quad (2)$$

where,  $s_k$  and  $p_t$  are the transmit signal and the transmit power in the uplink, respectively,  $\eta_k \sim \mathcal{CN}(0, \sigma^2)$  denotes the additive white Gaussian noise (AWGN). The term  $w_k \in \mathbb{C}^M$  is the normalized beamforming vector at the AP, and  $\Phi_k = \text{diag}(e^{j\theta_{1,k}}, \dots, e^{j\theta_{M,k}})$  is a diagonal matrix that accounts for the phase shifts  $\theta_{m,k} \in [0, 2\pi]$  associated with the reflective elements of the IRS. Due to the high path loss of mm-wave transmissions, signals that are reflected more than once are subject to severe attenuations and are not considered in (2). Thus, the received signal-to-noise ratio (SNR) at timeslot  $k$  can be written as follows:

$$\text{SNR}_k = \frac{|(h_{r,k}^H \Phi_k G_k + h_{d,k}^H) w_k|^2}{\sigma^2} p_t, \quad (3)$$

where, the superscript  $H$  represents the hermitian. Moreover, let  $d_{i,k} = \sqrt{(z_r - z_i)^2 + \|q_k - q_i\|_2^2}$ , and  $d_{a,k} = \sqrt{(z_r - z_a)^2 + \|q_k - q_a\|_2^2}$  be the robot-IRS and robot-AP distances, respectively. Then, channel vectors  $h_{r,k}$  and  $h_{d,k}$  can be modeled as follows:

$$h_{r,k} = \sqrt{\rho d_{i,k}^{-\nu}} \tilde{h}_{r,k}, \quad (4)$$

$$h_{d,k} = \sqrt{\rho d_{a,k}^{-\mu}} \tilde{h}_{d,k}, \quad (5)$$

where,  $\tilde{h}_{r,k} \sim \mathcal{CN}(0, I)$  and  $\tilde{h}_{d,k} \sim \mathcal{CN}(0, I)$  are complex gaussian vectors whose elements are independent and identical distributed (i.i.d) with zero means and unit variances. The term  $\rho$  is the path loss at the reference distance of 1 m, and  $\nu$  and  $\mu$  are the path loss exponents of the reflected and direct channels, respectively.

Finally, for fixed  $\Phi_k$ ,  $w_k$ , and position  $q_k$ , we obtain the data rate by using the Shannon's formula as follows:

$$\begin{aligned} r_k &= B_w \log_2 (1 + \text{SNR}_k) = \\ &B_w \log_2 \left( 1 + \frac{|(\sqrt{\rho d_{i,k}^{-\nu}} \tilde{h}_{r,k}^H \Phi_k G_k + \sqrt{\rho d_{a,k}^{-\mu}} \tilde{h}_{d,k}^H) w_k|^2}{\sigma^2} p_t \right), \end{aligned} \quad (6)$$

TABLE I: Summary of the notation.

AP	access point	IRS	intelligent reflective surface
$\mathbf{q}$	robot trajectory	$q_k$	robot's position in timeslot $k$
$q_s$	robot's starting position	$q_d$	robot's final position
$q_a$	AP's position	$q_i$	IRS's position
$z_a$	AP's height	$z_i$	IRS's height
$d_{a,k}$	robot-AP distance in timeslot $k$	$d_{i,k}$	robot-IRS distance in timeslot $k$
$\mathcal{O}$	Obstacle set	$q_{c,o}$	center's position of obstacle $o \in \mathcal{O}$
$K$	number of timeslots	$r_{min}$	minimum average data rate requirement
$D_{max}$	maximum distance that a robot can travel in a timeslot	$N$	number of antennas at the AP
$M$	number of reflective elements at the IRS	$G_k$	AP-IRS channel in timeslot $k$
$h_{r,k}$	robot-IRS channel in timeslot $k$	$h_{d,k}$	robot-AP channel in timeslot $k$
$\theta_{m,k}$	phase shift of reflective element $m$ in timeslot $k$	$\Phi_k$	phase shifts matrix in timeslot $k$
$w_k$	normalized beamforming vector at the AP in timeslot $k$	$B_w$	system bandwidth
$E$	total robot motion energy consumption	$E_k$	robot motion energy consumption in timeslot $k$
$\text{SNR}_k$	received SNR in timeslot $k$	$r_k$	achieved data rate in timeslot $k$
$\mathbf{r}$	achieved data rate vector for timeslots $k = 0, \dots, K$	$\bar{\mathbf{r}}$	achieved average data rate
$\widehat{\text{SNR}}_k^*$	estimated optimal SNR in timeslot $k$	$\bar{\mathbf{r}}^*$	optimal achieved data rate
$\bar{r}_{apx}^*$	concave approximation of the achieved average data rate	$\bar{r}_{map}$	achieved average data rate obtained by the radio map
$T_k$	trust region in timeslot $k$	$\tau$	trust region reduction parameter
$\hat{\nu}$	estimated robot-IRS path loss exponent	$\hat{\mu}$	estimated robot-AP path loss exponent
$\mathbf{q}_0$	initial solution for Algorithm 1 (RMAP)	$\mathbf{q}_j$	solution of Algorithm 1 (RMAP) at iteration $j$

where, (4) and (5) are used in (3) and  $B_w$  represents the system bandwidth. Let  $\mathbf{r} = [\mathbf{r}_0, \mathbf{r}_1, \dots, \mathbf{r}_K]$  be a vector, of which the elements represent the data rates at timeslots  $k = 0, 1, \dots, K$ . Thus, the average data rate for a trajectory  $\mathbf{q}$  is given by:

$$\bar{\mathbf{r}} = \frac{1}{K} \sum_{k=0}^K \mathbf{r}_k. \quad (7)$$

We can observe that  $\bar{\mathbf{r}}$  is a function of  $\Phi_k$ ,  $w_k$ , and  $q_k$ . The latter is included in  $d_{i,k}$ , and  $d_{a,k}$ . Thus, the robot's position and beamforming affect the data rate, which in turn affects the trajectory due to the QoS constraint. In the next section, we formulate the joint beamforming and trajectory optimization problem introduced in this section.

### III. PROBLEM FORMULATION

In this section, we formulate the problem introduced in Section II. Let  $\Phi = [\Phi_0, \Phi_1, \dots, \Phi_K]$  and  $\mathbf{w} = [w_0, w_1, \dots, w_K]$ , then the joint robot trajectory and beamforming problem can be



formulated as follows:

$$P1 : \min_{\mathbf{q}, \Phi, \mathbf{w}} E \quad (8a)$$

$$\text{s.t. } \bar{r} \geq r_{min}, \quad (8b)$$

$$\|q_k - q_{k-1}\|_2 \leq D_{max}, \quad k = 1, \dots, K, \quad (8c)$$

$$q_0 = q_s, \quad q_K = q_d, \quad (8d)$$

$$(q_k - q_{c,o})^T P_o^{-1} (q_k - q_{c,o}) \geq d_s, \quad \forall k, \forall o \in \mathcal{O}, \quad (8e)$$

$$\|w_k\|_2^2 \leq 1, \quad \forall k, \quad (8f)$$

$$\Phi_k = \text{diag} (e^{j\theta_{1k}}, \dots, e^{j\theta_{Mk}}), \quad \forall k, \quad (8g)$$

$$0 \leq \theta_{m,k} \leq 2\pi, \quad \forall m, \forall k, \quad (8h)$$

where, the objective function (8a) represents the total robot motion energy consumption along the trajectory given by (1). The first constraint (8b) represents the QoS requirement to complete the task, where  $\bar{r}$  is defined in (7) and  $r_{min}$  is the minimum required average data rate. Constraints (8c) allow the robot to move in a timeslot for a maximum distance of  $D_{max}$ , whereas (8d) fix the starting and the goal positions. To avoid collisions with obstacles, we include (8e). More precisely, as described in the previous section, each obstacle  $o \in \mathcal{O}$  can be described with ellipsoid shapes on the horizontal plane, with a center  $q_{c,o}$ , and a symmetric and positive definite matrix  $P_o$ . The latter defines the length of the axis and the rotation of the ellipse, and  $d_s \geq 1$  represents a safety distance between the robot and the obstacle. Finally, constraints (8f) and (8h) impose the norm of  $w_k$  to be at most one and  $\theta_{m,k}$  to be continuous, respectively. In practical implementations,  $\theta_{m,k}$ , with  $m = 1, \dots, M$  and  $k = 0, \dots, K$ , are discrete values that are quantized. However, we first assume  $\theta_{m,k}$  to be continuous and then, we can approximate the solution  $\theta_{m,k}^*$  to the closest discrete value based on Euclidean distance.

Problem  $P1$  is non-linear and non-convex. However, we show that, for each robot trajectory  $\mathbf{q}$ , it is possible to find closed-forms of  $\Phi$  and  $\mathbf{w}$  that maximize the average data rate. More precisely,  $\Phi_k$  and  $w_k$  are not contributing to the cost in (8a). Thus, when the right-hand side (RHS) of (8b) is maximized given a certain trajectory, we obtain a problem with a larger feasible region, of which the optimum is equivalent to that of  $P1$ . This equivalent problem of constrained trajectory optimization is solved in Section IV by using an SCO-based algorithm.

### A. Average Rate Maximization

In this section, we first find closed-form solutions of  $\Phi$  and  $w$  that maximize the average data rate  $\bar{r}$  for a fixed trajectory by solving the following problem:

$$\begin{aligned} P2 : \max_{\Phi, w} \bar{r} \\ \text{s.t. (8f), (8g), (8h),} \end{aligned} \quad (9a)$$

where,  $\bar{r}$  is given by (7). We can assume that the IRS and the AP are installed with LOS between them. Since in mm-wave communications the LOS path presents a much higher gain than the sum of NLOS paths, the IRS-AP channel can be approximated by a rank-one matrix [9]:

$$G_k = \sqrt{NM\rho d_{ia}^{-2}} \tilde{G}_k = \sqrt{NM}\gamma \tilde{a}_k \tilde{b}_k^T, \quad \forall k, \quad (10)$$

where,  $\gamma = \sqrt{\rho d_{ia}^{-2}}$ , and  $d_{ia}$  is the distance between the AP and the IRS that is fixed and does not depend on  $q_k$ . The path loss exponent that is associated with the LOS path between the AP and the IRS is two and  $\rho$  accounts for the path loss at the reference distance and antenna gain. The terms  $\tilde{a}_k \in \mathbb{C}^M$  and  $\tilde{b}_k \in \mathbb{C}^N$  are the normalized array response vectors in timeslot  $k$  associated with the IRS and the AP, respectively. These can be expressed as follows:

$$\tilde{a}_k = \frac{1}{\sqrt{M}} \left[ 1, e^{-j\frac{2\pi}{\lambda}l\alpha_k}, \dots, e^{-j\frac{2\pi}{\lambda}l(M-1)\alpha_k} \right], \quad (11)$$

$$\tilde{b}_k = \frac{1}{\sqrt{N}} \left[ 1, e^{-j\frac{2\pi}{\lambda}l\beta_k}, \dots, e^{-j\frac{2\pi}{\lambda}l(N-1)\beta_k} \right], \quad (12)$$

where,  $\alpha_k$  is the cosine of angle-of-arrival (AoA) and  $\beta_k$  is the cosine of angle-of-departure (AoD). The term  $\lambda$  is the carrier wavelength, whereas  $l$  is the antenna separation.

Maximizing P2 is equivalent to maximizing the received SNR in each timeslot  $k$  (3). Assuming  $\tilde{G}_k = \tilde{a}_k \tilde{b}_k^T$ , and  $\Phi_k = e^{j\alpha_k} \hat{\Phi}_k$ , this problem has a closed-form solution [9], which is given by:

$$\alpha_k^* = -\arg \left( \left( \tilde{b}_k^T \right)^H \tilde{h}_{d,k} \right), \quad (13)$$

$$\hat{\Phi}_k^* = \text{diag} \left( e^{-j\arg(g_{1,k})}, \dots, e^{-j\arg(g_{M,k})} \right), \quad (14)$$

$$w_k^* = \frac{\left( e^{j\alpha_k^*} \sqrt{\rho d_{i,k}^{-\nu}} \tilde{h}_{r,k}^H \hat{\Phi}_k^* G_k + \sqrt{\rho d_{a,k}^{-\mu}} \tilde{h}_{d,k}^H \right)^H}{\| e^{j\alpha_k^*} \sqrt{\rho d_{i,k}^{-\nu}} \tilde{h}_{r,k}^H \hat{\Phi}_k^* G_k + \sqrt{\rho d_{a,k}^{-\mu}} \tilde{h}_{d,k}^H \|_2}, \quad (15)$$

where,  $g_k = \sqrt{\rho d_{ia,k}^{-2}} (\tilde{h}_{r,k}^* \circ \tilde{a}_k)$  and  $(\circ)$  denotes the elementwise product. By putting (13), (14), and (15) into (3), we obtain the following optimal SNR expression for timeslot  $k$ :

$$\text{SNR}_k^* = \left( N|\rho||\gamma|^2 \|\tilde{h}_{r,k}\|_1^2 d_{i,k}^{-\nu} + 2\sqrt{N}|\rho|\gamma \|\tilde{h}_{r,k}^H\|_1 |\tilde{b}_k^T \tilde{h}_{d,k}| d_{i,k}^{-\nu/2} d_{a,k}^{-\mu/2} + \rho \|\tilde{h}_{d,k}\|_2^2 d_{a,k}^{-\mu} \right) \frac{p_t}{\sigma^2} = \left( A d_{i,k}^{-\nu} + B d_{i,k}^{-\nu/2} d_{a,k}^{-\mu/2} + C d_{a,k}^{-\mu} \right) \frac{p_t}{\sigma^2}, \quad (16)$$

where, in the last equality, we have highlighted the dependence of  $\text{SNR}_k^*$  on the robot position  $q_k$  through the terms  $d_{a,k}$  and  $d_{i,k}$ . However,  $\nu$  and  $\mu$  may rapidly change depending on the scattering environment and robot's position  $q_k$ . This can make the data rate model intractable for trajectory optimization in Section IV. For this reason, we proceed as follows: starting from (16), we first estimate  $\nu$  and  $\mu$ , and other parameters, i.e.,  $A$ ,  $B$ , and  $C$ , from a set of measurements by assuming them constants. Then, in Section IV, we use a radio map information to address the dependence between the path loss exponents and the robot's position.

More precisely, given a set of channel measurements we compute (13), (14), and (15) and construct a radio map that provides the averaged optimal  $\text{SNR}^*$  for each position. Then, we can estimate  $\hat{A} \geq 0$ ,  $\hat{B} \geq 0$ ,  $\hat{C} \geq 0$ ,  $\hat{\nu} \geq 0$ , and  $\hat{\mu} \geq 0$  by fitting (16) with the radio map. This procedure results in:

$$\widehat{\text{SNR}}_k^* = \left( \hat{A} d_{i,k}^{-\hat{\nu}} + \hat{B} d_{i,k}^{-\hat{\nu}/2} d_{a,k}^{-\hat{\mu}/2} + \hat{C} d_{a,k}^{-\hat{\mu}} \right) \frac{p_t}{\sigma^2}, \quad (17)$$

where,  $\hat{A}$ ,  $\hat{B}$ ,  $\hat{C}$ ,  $\hat{\nu}$ , and  $\hat{\mu}$  are the estimated parameters. This model has the advantages of analytical tractability of (16) for trajectory optimization and capturing the dependence on the scattering environment.

We can use (17) in (7) to obtain an estimation of the maximum data rate resulting from the beamforming optimization:

$$\begin{aligned} \bar{\mathbf{r}}^* &= \frac{1}{K} \sum_{k=0}^K \mathbf{r}_k^* = \frac{\mathbf{B}_w}{K} \sum_{k=0}^K \log_2 \left( 1 + \widehat{\text{SNR}}_k^* \right) = \\ &= \frac{\mathbf{B}_w}{K} \sum_{k=0}^K \log_2 \left( 1 + \left( \hat{A} d_{i,k}^{-\hat{\nu}} + \hat{B} d_{i,k}^{-\hat{\nu}/2} d_{a,k}^{-\hat{\mu}/2} + \hat{C} d_{a,k}^{-\hat{\mu}} \right) \frac{p_t}{\sigma^2} \right), \end{aligned} \quad (18)$$

where,  $\mathbf{r}_k^*$  is the optimized data rate at timeslot  $k$ . Finally, by replacing the RHS of (8b) with (18), we can decouple the beamforming and the trajectory optimization obtaining the

following problem:

$$P3 : \min_{\mathbf{q}, \Phi, \mathbf{w}} E \quad (19a)$$

$$\text{s.t. } \bar{\mathbf{r}}^* \geq \mathbf{r}_{\min}, \quad (19b)$$

$$(8c), (8d), (8e),$$

where,  $E$  in (23a) is the robot energy consumption that is given by (1). This problem is equivalent to P1, but it considers the estimated optimal data rate,  $\bar{\mathbf{r}}^*$ .

#### IV. TRAJECTORY OPTIMIZATION

In this section, we provide an algorithm to solve problem  $P3$  that, as introduced in Section III-A, is a trajectory optimization problem equivalent to  $P1$ . We first derive the following: *Lemma 1*: Given  $c_1 \geq 0$ ,  $c_2 \geq 0$ , and  $c_3 \geq 0$ , the objective function of  $P3$  (23a) is a convex function of  $\mathbf{q}$ .

*Proof.* We prove Lemma 1 by induction. Let  $E|_{K=n}$  be the energy consumption along the path (1) when  $K = n$ :  $\sum_{k=1}^n c_1 \frac{\|q_k - q_{k-1}\|_2^2}{\Delta_t} + c_2 \|q_k - q_{k-1}\|_2 + c_3 \Delta_t$ . We first prove that  $E|_{K=1}$  is convex and then, by assuming that convexity holds for  $E|_{K=n-1}$  we prove that  $E|_{K=n}$  is a convex function of  $\mathbf{q} = [q_0, \dots, q_n]$ . It is easy to show that  $E|_{K=1} = c_1 \frac{\|q_1 - q_0\|_2^2}{\Delta_t} + c_2 \|q_1 - q_0\|_2 + c_3 \Delta_t$  is a convex function of  $q_0$  and  $q_1$  because it consists of the sum of two convex functions, i.e.,  $c_1 \frac{\|q_1 - q_0\|_2^2}{\Delta_t}$  and  $c_2 \|q_1 - q_0\|_2$ , and a constant term. Assume that  $E|_{K=n-1}$  is convex, then we have that  $E|_{K=n} = E|_{K=n-1} + c_1 \frac{\|q_n - q_{n-1}\|_2^2}{\Delta_t} + c_2 \|q_n - q_{n-1}\|_2 + c_3 \Delta_t$ . By following the same reasoning, we can observe that  $E|_{K=n}$  is the sum of three convex functions of  $\mathbf{q} = [q_0, \dots, q_n]$ :  $E|_{K=n-1}$  that is convex by hypothesis,  $\frac{\|q_n - q_{n-1}\|_2^2}{\Delta_t}$ , and  $c_2 \|q_n - q_{n-1}\|_2$ .  $\square$

However,  $P3$  is non-convex because the RHS of (19b) and (8e) are not concave functions of  $q_k$ . For this reason, we perform a convex local approximation of these two constraints and solve the problem iteratively by using an SCO algorithm. Starting from constraint (19b), we have the following lemma:

*Lemma 2*: Given  $\bar{A} \geq 0$ ,  $\bar{B} \geq 0$ ,  $\bar{C} \geq 0$ ,  $\bar{\nu} \geq 0$ , and  $\bar{\mu} \geq 0$ ,  $\bar{\mathbf{r}}^*$  is a convex function of  $d_{a,k}$  and  $d_{i,k}$  with  $k = 0, \dots, K$ .

*Proof.* See Appendix A.  $\square$

Thus, since any convex function can be lower-bounded by its first-order Taylor expansion, we have that  $\bar{\mathbf{r}}^* \geq \bar{\mathbf{r}}_{apx}^*$ . The latter ( $\bar{\mathbf{r}}_{apx}^*$ ) is the first-order Taylor expansion of  $\bar{\mathbf{r}}^*$  at expansion points  $d_{a,0,k}$  and  $d_{i,0,k}$  and is given by:

$$\bar{\mathbf{r}}_{apx}^* = \frac{\mathbf{B}_w}{K} \sum_{k=0}^K \log_2 \left( 1 + \left( \bar{A} d_{i,0,k}^{-\bar{\nu}} + \bar{B} d_{i,0,k}^{-\bar{\nu}/2} d_{a,0,k}^{-\bar{\mu}/2} + \bar{C} d_{a,0,k}^{-\bar{\mu}} \right) \frac{p_t}{\sigma^2} \right) + \nabla \bar{\mathbf{r}}^* \Big|_{(d_{a,0,k}, d_{i,0,k})}^T \begin{bmatrix} d_{a,k} - d_{a,0,k} \\ d_{i,k} - d_{i,0,k} \end{bmatrix}. \quad (20)$$

The term  $\nabla \bar{\mathbf{r}}^*$  is the gradient of  $\bar{\mathbf{r}}^*$  with respect to  $d_{a,k}$  and  $d_{i,k}$  and can be written as follows:

$$\nabla \bar{\mathbf{r}}^* = \frac{\mathbf{B}_w}{K} \sum_{k=0}^K \begin{bmatrix} \frac{\left( -\bar{\nu} \bar{A} d_{i,k}^{-\bar{\nu}-1} - \bar{\nu}/2 \bar{B} d_{i,k}^{-\bar{\nu}/2-1} d_{a,k}^{-\bar{\mu}/2} \right) \frac{p_t}{\sigma^2}}{\ln 2 \left( 1 + \left( \bar{A} d_{i,k}^{-\bar{\nu}} + \bar{B} d_{i,k}^{-\bar{\nu}/2} d_{a,k}^{-\bar{\mu}/2} + \bar{C} d_{a,k}^{-\bar{\mu}} \right) \frac{p_t}{\sigma^2} \right)} \\ \frac{\left( -\bar{\mu} \bar{C} d_{a,k}^{-\bar{\mu}-1} - \bar{\mu}/2 \bar{B} d_{i,k}^{-\bar{\nu}/2} d_{a,k}^{-\bar{\mu}/2-1} \right) \frac{p_t}{\sigma^2}}{\ln 2 \left( 1 + \left( \bar{A} d_{i,k}^{-\bar{\nu}} + \bar{B} d_{i,k}^{-\bar{\nu}/2} d_{a,k}^{-\bar{\mu}/2} + \bar{C} d_{a,k}^{-\bar{\mu}} \right) \frac{p_t}{\sigma^2} \right)} \end{bmatrix}. \quad (21)$$

We now consider the following lemma:

*Lemma 3:* Given non-negative parameters  $\bar{A}$ ,  $\bar{B}$ ,  $\bar{C}$ ,  $\bar{\nu}$ , and  $\bar{\mu}$ ,  $\bar{\mathbf{r}}_{apx}^*$  is a concave function of  $q_k$ .

*Proof.* See Appendix B.  $\square$

Thus, in a small neighborhood of  $d_{a,0,k}$  and  $d_{i,0,k}$ , we can approximate  $\bar{\mathbf{r}}^*$  with a concave function of  $q_k$  given by  $\bar{\mathbf{r}}_{apx}^*$ . The same reasoning can be applied to (8e) leading to the following inequality:

$$(q_k - q_{c,o})^T P_o^{-1} (q_k - q_{c,o}) \geq (q_{0,k} - q_{c,o})^T P_o^{-1} (q_{0,k} - q_{c,o}) + (q_{0,k} - q_{c,o})^T P_o^{-1} (q_k - q_{0,k}) \quad (22)$$

where, the RHS is the first-order Taylor expansion of (8e) with respect to  $q_k$  at local point  $q_{0,k}$ . This is an affine function of  $q_k$ . Finally, by considering (20), (22) and an initial feasible trajectory  $\mathbf{q}_0$ , we can solve a sequence of local convex approximations of  $P3$  as shown in Algorithm 1

(*RMAP*) that provides an upper bound to the solution of *P3*. At each iteration  $j$ , *RMAP* solves the following problem:

$$P4 : \min_{\mathbf{q}_j} \sum_{k=1}^K c_1 \frac{\|q_{j,k} - q_{j,k-1}\|_2^2}{\Delta_t} + c_2 \|q_{j,k} - q_{j,k-1}\|_2 + c_3 \Delta_t \quad (23a)$$

$$\text{s.t. } \bar{\mathbf{r}}_{apx,j}^* \geq \mathbf{r}_{min}, \quad (23b)$$

$$\|q_{j,k} - q_{j,k-1}\|_2 \leq D_{max}, \quad \forall k, \quad (23c)$$

$$q_0 = q_s, \quad q_K = q_d, \quad (23d)$$

$$\|q_{j,k} - q_{j-1,k}\|_2 \leq T_k, \quad \forall k, \quad (23e)$$

$$(q_{j-1,k} - q_{c,o})^T P_o^{-1} (q_{j-1,k} - q_{c,o}) + \\ (q_{j-1,k} - q_{c,o})^T P_o^{-1} (q_{j,k} - q_{j-1,k}) \geq 1, \quad \forall k, o, \quad (23f)$$

where,  $\mathbf{q}_j = [q_{j,0}, q_{j,1}, \dots, q_{j,K}]$  and  $\mathbf{q}_{j-1} = [q_{j-1,0}, q_{j-1,1}, \dots, q_{j-1,K}]$  are the solutions of *P4* at iteration  $j$  and  $j-1$ , respectively. More precisely,  $\mathbf{q}_{j-1}$  represents the local point at which the approximations at iteration  $j$  of constraints (19b) and (8e) are computed. These approximations are valid in a trust region of  $\mathbf{q}_{j-1}$  that is defined by constraint (23e). The trust region size  $T_k$  may differ by timeslot. Note that the expansion points of  $\bar{\mathbf{r}}^*$  can be obtained from  $q_{j-1,k}$ , as  $d_{a,j-1,k} = \sqrt{(z_r - z_a)^2 + \|q_{j-1,k} - q_a\|_2^2}$  and  $d_{i,j-1,k} = \sqrt{(z_r - z_i)^2 + \|q_{j-1,k} - q_i\|_2^2}$ . Problem *P4* is convex and it can be solved quickly by interior-point methods.

As introduced in Section III-A,  $\bar{\mathbf{r}}^*$  and its approximation ( $\bar{\mathbf{r}}_{apx}^*$ ) can still diverge from the true data rate, especially when abrupt LOS-NLOS transitions occur. Thus, in *RMAP* we introduce a solution update mechanism that differs from conventional SCO-based algorithms. The goal is to keep the feasibility of the solution at iteration  $j$  also with respect to the measured data rate obtained from the radio map and not only to its convex approximation ( $\bar{\mathbf{r}}_{apx,j}^*$ ). More precisely, let  $\mathbf{r}_{map,j}$  be a vector of  $K$  elements, each of which consists of the measured data rate with optimized beamforming vectors at  $q_{jk}$ . Let  $\bar{\mathbf{r}}_{map,j}$  be the average of  $\mathbf{r}_{map,j}$  along the trajectory. Then, at iteration  $j$ , *RMAP* updates the solution, only if  $\bar{\mathbf{r}}_{map,j} \geq \mathbf{r}_{min}$ , otherwise it keeps the previous solution, i.e.,  $\mathbf{q}_j = \mathbf{q}_{j-1}$ . Furthermore, to obtain following feasible solutions, the algorithm reduces the trust-region  $T_k$  of a factor  $0 \leq \tau < 1$ , where  $k$  represents the timeslot in which the measured data rate from the radio map drops the most with respect to the previous trajectory solution:  $k = \underset{k}{\operatorname{argmax}} \mathbf{r}_{map,kj-1} - \mathbf{r}_{map,kj}$ .

---

**Algorithm 1** *Radio Map Assisted Planning (RMAP)*


---

**Initial solution:**

- 1:  $j=0$
- 2: Find an initial feasible solution  $\mathbf{q}_j$
- 3: Compute the motion energy consumption  $E_j$  corresponding to  $\mathbf{q}_j$  as in (23a)

**SCO:**

- 4: **repeat**
  - 5:    $j = j + 1$
  - 6:   Obtain  $\mathbf{q}_j$  and  $E_j$  by solving  $P4$  with local points  $\mathbf{q}_{j-1}$
  - 7:   **if**  $\bar{r}_{map,j} < r_{min}$  **then**
  - 8:      $\mathbf{q}_j = \mathbf{q}_{j-1}$  and  $E_j = E_{j-1}$
  - 9:      $T_k = \tau T_k$  with,  $0 \leq \tau < 1$  and  $k = \underset{k}{\operatorname{argmax}} r_{map,kj-1} - r_{map,kj}$
  - 10:   **else**
  - 11:     **if**  $\frac{E_j - E_{j-1}}{E_{j-1}} \leq \epsilon$  **then**
  - 12:       **break**
  - 13:     **end if**
  - 14:   **end if**
  - 15: **until**  $j \geq N_{it}$
- 

Hence, the algorithm maintains the feasibility with respect to both  $\bar{r}^*$  and  $\bar{r}_{map}$ . The analytical tractability of the former is used to optimize the trajectory and understand the behavior of the data rate with respect to the distances between the robot, the AP, and the IRS. The latter,  $\bar{r}_{map}$ , is used to capture the NLOS and LOS transitions created by the obstacles. The algorithm stops if the sequence of solutions converges or when a maximum number of iterations ( $N_{it}$ ) is reached. More precisely, we can prove that the algorithm converges and, under some conditions, it converges to a Karush-Kuhn-Tucker (KKT) point of  $P3$ .

**Theorem 1.** *The sequence of solutions provided by RMAP is non-increasing and it converges. Moreover, if at each iteration  $j$  we have that  $\bar{r}_{map,j} \geq r_{min}$ , RMAP converges to a KKT point of  $P3$ .*

*Proof.* The sequence of solutions provided by RMAP is non increasing because, the solution of  $P4$  at iteration  $j - 1$ ,  $\mathbf{q}_{j-1}$ , is a feasible solution of minimization problem  $P4$  at iteration  $j$ . For the rest of the proof, see AppendixC and Appendix D.  $\square$

**Proposition 1.** *If the average measured data rate corresponding to the initial solution satisfies  $\bar{r}_{map,0} \geq r_{min}$ , then the solution to which RMAP converges satisfies this constraint as well.*

This is a direct consequence of Lines 7-9 of RMAP and Theorem 1. Namely, if  $\bar{r}_{map,j} < r_{min}$  then  $\mathbf{q}_j = \mathbf{q}_{j-1}$ . Moreover, assuming that the initial solution satisfies  $\bar{r}_{map,0} \geq r_{min}$  and RMAP

converges to a solution, this solution must satisfy the above constraint.

In general, the quality of a solution of SCO-based algorithms depends also on the initial solution. In this work, we obtain  $q_0$  by computing the shortest path on a time expanded graph as done in [30]. The edges and vertices of the graph are defined on a discrete set of positions that are free from obstacles. In each timeslot, a robot may either stay at a vertex or move to an adjacent one. The distance between the vertex is set according to the robot's maximum speed. On this graph, the costs of the edges are set to generate two different initial solutions. The first one minimizes the motion energy consumption (ME) and the second solution maximizes the data rate (MR). The radio map is used to obtain the SNR and the data rate for the positions corresponding to vertices and edges. Then, *RMAP* uses the minimum energy initial solution if this is feasible ( $\bar{r}_{map,0} \geq r_{min}$  and  $\bar{r}_{apx}^* \geq r_{min}$ ) and the maximum data rate initial solution, otherwise. If also the latter is not feasible, the algorithm declares infeasibility.

## V. NUMERICAL RESULTS

In this section, we provide a numerical validation of *RMAP* for solving *P3*. For our simulations, we consider a  $50 \times 30$  m<sup>2</sup> rectangular-shaped indoor scenario. The robot's starting position is  $[9.5, 15.5]$ , whereas the destination is  $[40.5, 14.5]$ . There are an AP and an IRS placed at  $[25, 30]$  and  $[25, 0]$ , respectively, operating in the 60 GHz band as in [27], with bandwidth  $B_w = 200$  MHz. The height of the AP is 5 m, whereas, we set the heights of the IRS and the robot's antenna to 2.5 and 0.5 m, respectively. For sake of clarity, we first present results for a scenario consisting of four ellipse obstacles that are placed as in Fig. 2, represented by grey shaded areas (*base scenario*). This scenario includes several robot-AP and robot-IRS channel conditions, i.e., LOS and NLOS positions. Then, we present results that are averaged over ten instances in which 20 obstacles are randomly placed (*random scenario*). In both scenarios, obstacles have length, width, and height of 6 m, 4 m, and 2 m, respectively.

Similar to [27], the path loss at a reference distance of 1 m is 68 dB, and the path loss exponent of the robot-AP and robot-IRS channels are set to 2 for LOS, and 4.5 for NLOS. Without loss of generality the antenna gain of the reflective elements are set to 0 dBi. Moreover, we set the transmit and the noise powers to 20 dBm, and  $-80$  dBm, respectively. We show the results, for several values of  $M$  and  $r_{min}$ , and, unless otherwise specified, we set the following parameters values:  $K = 30$ ,  $\tau = 0.5$ ,  $N = 16$ ,  $\Delta_t = 1$  s,  $v_{max} = 3$  m/s,  $d_s = 1.35$ ,  $N_{it} = 100$ ,  $\epsilon = 0.01$ ,  $T = 1$  m,  $c_1 = 4.39$ ,  $c_2 = 24.67$ , and  $c_3 = 14.77$  [17]. Finally, we can obtain (17) by estimating



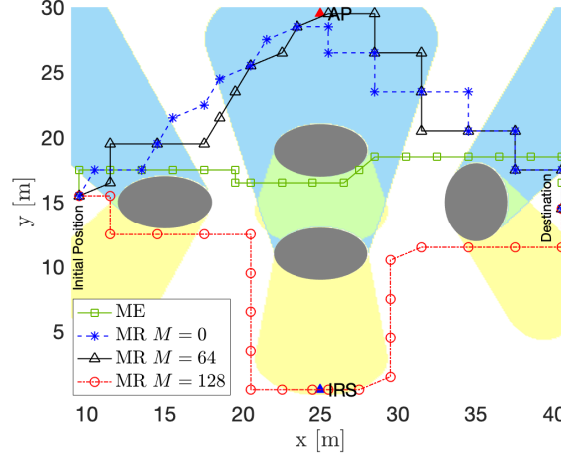


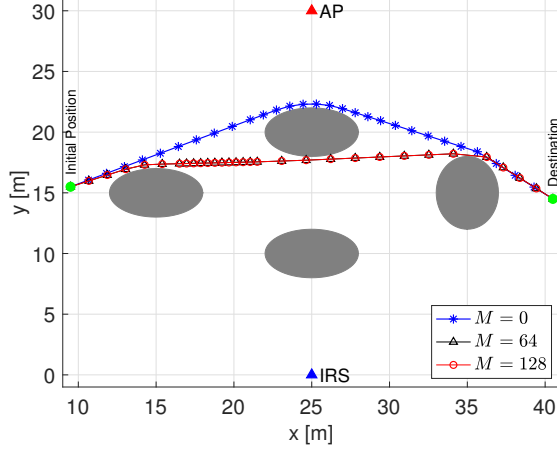
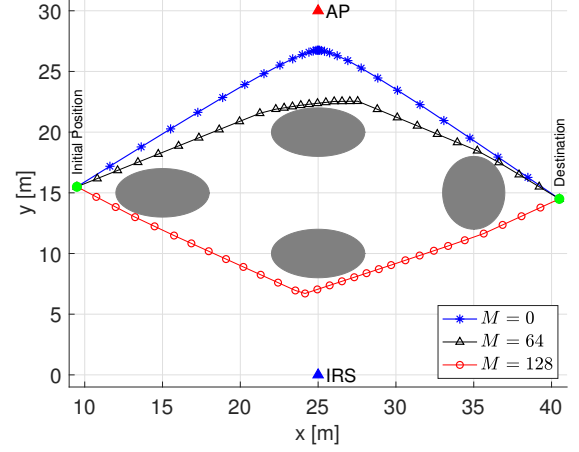
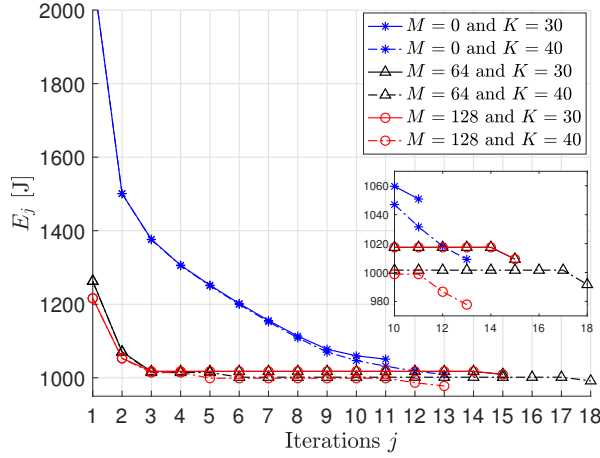
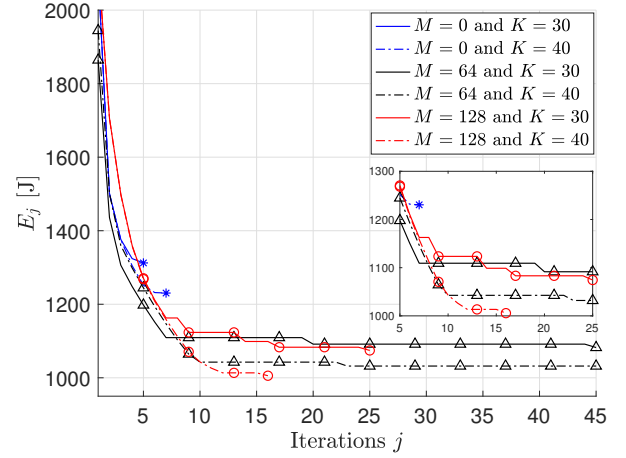
Fig. 2: Minimum energy (ME) and maximum data rate (MR) initial solutions for  $K = 30$  and several values of  $M$ . Yellow, blue, and green shaded positions are in NLOS with respect to the AP, the IRS, and both, respectively. The positions in the white area are in LOS with respect to both the IRS and the AP.

$\hat{A} \geq 0$ ,  $\hat{B} \geq 0$ ,  $\hat{C} \geq 0$ ,  $\hat{\nu} \geq 0$ , and  $\hat{\mu} \geq 0$  by fitting (16) on a radio map by solving a non-linear least squares problem. The radio map is obtained from the average of 10.000 channel measurements on a grid of  $500 \times 300$  points.

#### A. Base Scenario

In Fig. 2, we first show ME and MR initial solutions for several values of  $M$ . Note that MR initial solution considers trajectories that avoid NLOS areas with respect to either the AP or to the IRS depending on the number of reflective elements of the latter ( $M$ ).

In Fig. 3a we show robot trajectories resulting from *RMAP* for  $K = 30$ ,  $r_{min} = 2.0$  Gbps, and several values of  $M$ . For  $M = 0$ , we can observe that the robot avoids NLOS areas with respect to the AP, and *RMAP* uses initial solution MR. When  $M$  increases, the IRS enhances the coverage and the robot can find a trajectory with lower energy consumption ( $E$ ) by using initial solution ME. The resulting trajectory crosses the NLOS area with respect to both the AP and the IRS. Note that, for  $r_{min} = 2.0$  Gbps, values of  $M$  that are higher than 64 do not provide further gain, thus the trajectories for  $M = 64$  and  $M = 128$  coincide. This is not true when  $r_{min} = 2.5$  Gbps, for which the trajectories are shown in Fig. 3b. Specifically, when  $r_{min}$  increases, *RMAP* selects the MR initial solutions for all the values of  $M$  and the resulting paths are closer to the AP or the IRS to improve the coverage and increase the data rate. For  $M = 0$

(a)  $r_{min} = 2.0$  Gbps.(b)  $r_{min} = 2.5$  Gbps.Fig. 3: Robot trajectories to which *RMAP* converges for  $K = 30$ , and several values of  $M$  and  $r_{min}$ .(a)  $r_{min} = 2.0$  Gbps.(b)  $r_{min} = 2.5$  Gbps.Fig. 4: Energy consumption corresponding to the sequence of solutions  $\mathbf{q}_j$  provided by *RMAP* for several values of  $M$ ,  $r_{min}$ , and  $K$ .

and  $M = 64$  the robot trajectories avoid completely NLOS areas with respect to the AP, whereas, for  $M = 128$ , paths that are closer to the IRS provide higher data rates. We can also observe that the robot decreases the speed when the data rate is higher. More precisely, in LOS positions that are closer to the AP and the IRS, the robot travels for a smaller distance in each timeslot to exploit the better coverage.

In general,  $E$  increases for higher values of  $r_{min}$  and decreases when  $M$  and  $K$  increase.

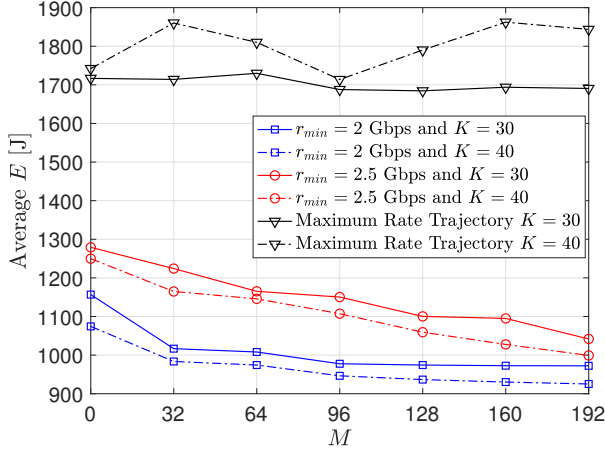


Fig. 5: Average  $E$  corresponding to solutions of  $RMAP$  and maximum data rate trajectories for several values of  $M$ ,  $r_{min}$ , and  $K$ .

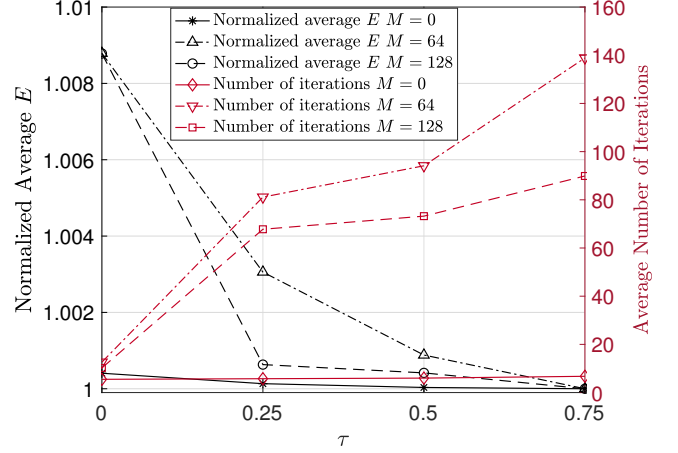


Fig. 6: Normalized average  $E$  and number of iterations within which  $RMAP$  converges for several values of  $M$ ,  $\tau$ ,  $K = 30$  and  $r_{min} = 2.5$  Gbps.

This can be better observed in Fig. 4a and Fig. 4b where we show  $E$  corresponding to the sequence of solutions  $\mathbf{q}_j$  ( $E_j$ ) provided by  $RMAP$  for  $r_{min} = 2.0$  Gbps and  $r_{min} = 2.5$  Gbps, respectively. First, we can observe that, by increasing  $M$ ,  $RMAP$  converges to paths with lower  $E$ . The energy consumption decreases also when  $K$  increases. Specifically, for a fixed value of  $\Delta_t$ , higher values of  $K$  correspond to longer deadlines and the robot can decrease the speed along the trajectory to reach the destination. Then, given (1), a lower speeds correspond to lower values of  $E$ . Finally, we can observe that  $E_j$  is non-increasing and  $RMAP$  converges in few iterations. As explained and shown better in the following section, the number of iterations within which  $RMAP$  converges depends on the value of  $\tau$ .

### B. Random Scenario

In this section, we present results that are averaged over 10 instances in which  $N_o = 20$  obstacles are randomly placed. The dimensions of the obstacles and the area are the same that are used for Section V-A, as well as the robot's starting position and destination. In Fig. 5, we show the average energy consumption corresponding to the trajectory resulting from  $RMAP$  for several values of  $M$ ,  $K$  and  $r_{min}$ . Moreover, we show the average  $E$  corresponding to trajectories of the robot that maximize the data rate under time and collision avoidance constraints. Note that these are feasible solutions of  $P3$ . Specifically, maximum data rate trajectories are obtained by

solving a modified version of P3, where the RHS of (19b) represents the objective function of the problem. This problem is solved by using a SCO-based algorithm where, as done in Section IV for P3, the objective function and the RHS of (8e) are approximated by convex functions. We can observe that, for both  $r_{min} = 2.0$  Gbps and  $r_{min} = 2.5$  Gbps, *RMAP* can reduce dramatically the average  $E$  with respect to a maximum data rate approach, with a gain that is close to 100% for  $r_{min} = 2.0$  Gbps. Moreover, Fig. 5 shows that the average  $E$  of the robot is monotonically decreasing as a function of  $M$ . Specifically, by increasing the number of reflective elements at the IRS we enhance the coverage, and the number of feasible trajectories increases. While for  $r_{min} = 2.5$  Gbps the increasing of  $M$  results in a constant decrease of  $E$ , we note that values of  $M$  that are higher than 32 do not provide significant gains for  $r_{min} = 2.0$  Gbps. Further gains are obtained by increasing the values of  $K$  as also explained in Section V-A. These observations do not hold for maximum data rate trajectories for which the solutions have not monotonic decreasing behaviors with respect to  $M$  and  $K$ .

Finally, in Fig. 6 we show the effects of parameter  $\tau$  on the number of iterations within which *RMAP* converges. Moreover, we show the average  $E$  corresponding to the solutions within which *RMAP* converges for several values of  $\tau$ . These are normalized to the solutions that are obtained for  $\tau = 0.75$ . As explained in Section IV, in each iteration of *RMAP* for which the solution does not satisfy  $\bar{r}_{map,j} \geq r_{min}$ , we multiply the trust region size, of the timeslot where the data rate drops the most, by  $\tau$ . Specifically, when  $\tau$  is smaller, the sizes of the trust regions may decrease faster leading to a faster algorithm convergence. This can be observed in Fig. 6, which shows a tradeoff between the number of iterations within which *RMAP* converges and the quality of the solution. The latter improves when  $\tau$  grows leading to lower values of average  $E$ . However, when  $\tau = 0$ , *RMAP* provides solutions in fewer iterations and negligible loss ( $\leq 1\%$ ) with respect to the ones provided for  $\tau = 0.75$ .

## VI. CONCLUSION

In this work, we have proposed a novel robot trajectory optimization problem with QoS constrained communications for minimizing the motion energy consumption. The robot must avoid collisions with obstacles, reach the destination within a deadline, and transmit data to an AP operating at mm-wave frequency bands and assisted by an IRS. The uplink transmission is subject to a minimum average data rate. To the best of our knowledge, energy-efficient trajectory planning problems for wirelessly connected robots have not been considered for

mm-wave communications. We have proposed a solution that accounts for the challenging signal propagation conditions at such high frequencies and the mutual dependence between the channel conditions and the robot trajectory. Specifically, by exploiting the mm-wave propagation characteristics, we have decoupled the beamforming (at the AP and IRS) and the trajectory optimization problems. The latter is solved by an SCO-based algorithm (*RMAP*) for which the convergence is proved. *RMAP* can deal with sudden data rate drops due to LOS-NLOS transitions by using the information that is stored in a radio map. Given this information, *RMAP* can find trajectories that avoid obstacles and poorly connected areas for satisfying data rate requirements.

We have shown trajectories and corresponding energy consumptions at which the algorithm converges for several scenarios and system parameters, e.g., number of reflective elements at the IRS, QoS requirements, and time deadlines. The algorithm converges in few iterations to a solution that can dramatically reduce the energy consumption with respect to trajectories that maximize the data rate. Finally, we have shown how, by increasing the number of IRS's reflective elements, we can improve the coverage and the energy consumption of the robot.

## APPENDIX A

To prove Lemma 2, we prove that  $r_k^*$ , which is the estimated data rate at timeslot  $k$ , is a convex function of  $d_{i,k}$  and  $d_{a,k}$ . Then,  $\bar{r}^*$  is convex because it is a sum of convex functions. We first compute the partial derivatives of  $r_k^*$  with respect to  $d_{i,k}$  and  $d_{a,k}$ . These are given by:

$$\frac{\partial r_k^*}{\partial d_{i,k}} = \frac{\left( -\bar{\nu} \bar{A} d_{i,k}^{-\bar{\nu}-1} - \bar{\nu}/2 \bar{B} d_{i,k}^{-\bar{\nu}/2-1} d_{a,k}^{-\bar{\mu}/2} \right) \frac{p_t}{\sigma^2}}{F_k}, \quad (24)$$

$$\frac{\partial r_k^*}{\partial d_{a,k}} = \frac{\left( -\bar{\mu} \bar{C} d_{a,k}^{-\bar{\mu}-1} - \bar{\mu}/2 \bar{B} d_{i,k}^{-\bar{\nu}/2} d_{a,k}^{-\bar{\mu}/2-1} \right) \frac{p_t}{\sigma^2}}{F_k}, \quad (25)$$

where,  $F_k = \ln(2) \left( 1 + \left( \bar{A} d_{i,k}^{-\bar{\nu}} + \bar{B} d_{i,k}^{-\bar{\nu}/2} d_{a,k}^{-\bar{\mu}/2} + \bar{C} d_{a,k}^{-\bar{\mu}} \right) \frac{p_t}{\sigma^2} \right) > 0$ . Then, the second order partial derivatives are given by:

$$\begin{aligned} \frac{\partial^2 r_k^*}{\partial d_{i,k}^2} &= \frac{\left( \bar{\nu}(\bar{\nu}+1) \bar{A} d_{i,k}^{-\bar{\nu}-2} + \bar{\nu}/2(\bar{\nu}/2+1) \bar{B} d_{i,k}^{-\bar{\nu}/2-2} d_{a,k}^{-\bar{\mu}/2} \right) F_k \frac{p_t}{\sigma^2}}{F_k^2} \\ &\quad - \frac{\ln(2) \left( -\bar{\nu} \bar{A} d_{i,k}^{-\bar{\nu}-1} - \bar{\nu}/2 \bar{B} d_{i,k}^{-\bar{\nu}/2-1} d_{a,k}^{-\bar{\mu}/2} \right)^2 \frac{p_t^2}{\sigma^4}}{F_k^2}, \end{aligned} \quad (26)$$

$$\begin{aligned} \frac{\partial^2 \mathbf{r}_k^*}{\partial d_{a,k}^2} &= \frac{\left( \bar{\mu}(\bar{\mu} + 1) \bar{C} d_{a,k}^{-\bar{\mu}-2} + \bar{\mu}/2(\bar{\mu}/2 + 1) \bar{B} d_{i,k}^{-\bar{\nu}/2} d_{a,k}^{-\bar{\mu}/2-2} \right) F_k \frac{p_t}{\sigma^2}}{F_k^2} \\ &\quad - \frac{\ln(2) \left( -\bar{\mu} \bar{C} d_{a,k}^{-\bar{\mu}-1} - \bar{\mu}/2 \bar{B} d_{i,k}^{-\bar{\nu}/2} d_{a,k}^{-\bar{\mu}/2-1} \right)^2 \frac{p_t^2}{\sigma^4}}{F_k^2}, \end{aligned} \quad (27)$$

$$\begin{aligned} \frac{\partial^2 \mathbf{r}_k^*}{\partial d_{i,k} \partial d_{a,k}} &= \frac{\left( (\bar{\mu}/2)(\bar{\nu}/2) \bar{B} d_{i,k}^{-\bar{\nu}/2-1} d_{a,k}^{-\bar{\mu}/2-1} \right) F_k \frac{p_t}{\sigma^2}}{F_k^2} - \\ &\quad \frac{\ln(2) \left( -\bar{\nu} \bar{A} d_{i,k}^{-\bar{\nu}-1} - \bar{\nu}/2 \bar{B} d_{i,k}^{-\bar{\nu}/2-1} d_{a,k}^{-\bar{\mu}/2} \right) \frac{p_t^2}{\sigma^4}}{F_k^2} \times \\ &\quad \frac{\left( -\bar{\mu} \bar{C} d_{a,k}^{-\bar{\mu}-1} - \bar{\mu}/2 \bar{B} d_{i,k}^{-\bar{\nu}/2} d_{a,k}^{-\bar{\mu}/2-1} \right) \frac{p_t^2}{\sigma^4}}{F_k^2}. \end{aligned} \quad (28)$$

We observe that  $\frac{\partial^2 \mathbf{r}_k^*}{\partial d_{i,k}^2} > 0$ ,  $\frac{\partial^2 \mathbf{r}_k^*}{\partial d_{a,k}^2} > 0$  and  $\frac{\partial^2 \mathbf{r}_k^*}{\partial d_{i,k}^2} \frac{\partial^2 \mathbf{r}_k^*}{\partial d_{a,k}^2} - \left( \frac{\partial^2 \mathbf{r}_k^*}{\partial d_{i,k} \partial d_{a,k}} \right)^2 > 0$ . Therefore, the Hessian is positive definite and  $\mathbf{r}_k^*$  is a convex function of  $d_{i,k}$  and  $d_{a,k}$ .

## APPENDIX B

We prove Lemma 3 by following the same reasoning of Appendix A. Note that  $\bar{\mathbf{r}}_{apx}^*$  in (20) is the sum of  $K + 1$  functions each of them depending only on the robot's position at timeslot  $k$ :

$$\begin{aligned} \bar{\mathbf{r}}_{apx}^* &= \frac{1}{K} \sum_{k=0}^K \mathbf{r}_{app,k}^* = \\ &\quad \frac{1}{K} \sum_{k=0}^K B_w \log_2 \left( 1 + \left( \bar{A} d_{i,0,k}^{-\bar{\nu}} + \bar{B} d_{i,0,k}^{-\bar{\nu}/2} d_{a,0,k}^{-\bar{\mu}/2} + \bar{C} d_{a,0,k}^{-\bar{\mu}} \right) \frac{p_t}{\sigma^2} \right) \\ &\quad - \frac{\partial \mathbf{r}_k^*}{\partial d_{a,k}} \Big|_{(d_{a,0,k}, d_{i,0,k})} d_{a,0,k} - \frac{\partial \mathbf{r}_k^*}{\partial d_{i,k}} \Big|_{(d_{a,0,k}, d_{i,0,k})} d_{i,0,k} \\ &\quad + \frac{\partial \mathbf{r}_k^*}{\partial d_{a,k}} \Big|_{(d_{a,0,k}, d_{i,0,k})} \sqrt{(z_r - z_a)^2 + (x_k - x_a)^2 + (y_k - y_a)^2} \\ &\quad + \frac{\partial \mathbf{r}_k^*}{\partial d_{i,k}} \Big|_{(d_{a,0,k}, d_{i,0,k})} \sqrt{(z_r - z_i)^2 + (x_k - x_i)^2 + (y_k - y_i)^2}, \end{aligned} \quad (29)$$

where,  $\frac{\partial \mathbf{r}_k^*}{\partial d_{i,k}} < 0$  and  $\frac{\partial \mathbf{r}_k^*}{\partial d_{a,k}} < 0$  are given by (24) and (25), respectively. Note that in (29) we have replaced  $q_k$  with  $[x_k, y_k]$ . Let us define  $D_k = \sqrt{(z_r - z_a)^2 + (x_k - x_a)^2 + (y_k - y_a)^2}$ , then, we can compute the partial derivatives of  $\mathbf{r}_{app,k}^*$  with respect to  $x_k$  and  $y_k$  as follows:

$$\frac{\partial \mathbf{r}_{app,k}^*}{\partial x_k} = \frac{\partial \mathbf{r}_k^*}{\partial d_{a,k}} \Big|_{(d_{a,0,k}, d_{i,0,k})} \frac{(x_k - x_a)}{D_k} + \frac{\partial \mathbf{r}_k^*}{\partial d_{i,k}} \Big|_{(d_{a,0,k}, d_{i,0,k})} \frac{(x_k - x_i)}{D_k}, \quad (30)$$

$$\frac{\partial \mathbf{r}_{app,k}^*}{\partial y_k} = \frac{\partial \mathbf{r}_k^*}{\partial d_{a,k}} \Big|_{(d_{a,0,k}, d_{i,0,k})} \frac{(y_k - y_a)}{D_k} + \frac{\partial \mathbf{r}_k^*}{\partial d_{i,k}} \Big|_{(d_{a,0,k}, d_{i,0,k})} \frac{(y_k - y_i)}{D_k}, \quad (31)$$

The second order partial derivatives are given by:

$$\begin{aligned} \frac{\partial^2 \mathbf{r}_{app,k}^*}{\partial x_k^2} &= \frac{\partial \mathbf{r}_k^*}{\partial d_{a,k}} \Big|_{(d_{a,0,k}, d_{i,0,k})} \frac{(y_k - y_a)^2 + (z_k - z_a)^2}{D_k^3} + \\ &\quad \frac{\partial \mathbf{r}_k^*}{\partial d_{i,k}} \Big|_{(d_{a,0,k}, d_{i,0,k})} \frac{(y_k - y_i)^2 + (z_k - z_i)^2}{D_k^3}, \end{aligned} \quad (32)$$

$$\begin{aligned} \frac{\partial^2 \mathbf{r}_{app,k}^*}{\partial y_k^2} &= \frac{\partial \mathbf{r}_k^*}{\partial d_{a,k}} \Big|_{(d_{a,0,k}, d_{i,0,k})} \frac{(x_k - x_a)^2 + (z_k - z_a)^2}{D_k^3} + \\ &\quad \frac{\partial \mathbf{r}_k^*}{\partial d_{i,k}} \Big|_{(d_{a,0,k}, d_{i,0,k})} \frac{(x_k - x_i)^2 + (z_k - z_i)^2}{D_k^3}, \end{aligned} \quad (33)$$

$$\begin{aligned} \frac{\partial^2 \mathbf{r}_{app,k}^*}{\partial x_k \partial y_k} &= \frac{\partial \mathbf{r}_k^*}{\partial d_{a,k}} \Big|_{(d_{a,0,k}, d_{i,0,k})} \frac{(x_k - x_a)(y_k - y_a)}{D_k^3} + \\ &\quad \frac{\partial \mathbf{r}_k^*}{\partial d_{i,k}} \Big|_{(d_{a,0,k}, d_{i,0,k})} \frac{(x_k - x_i)(y_k - y_i)}{D_k^3}, \end{aligned} \quad (34)$$

Note that  $\frac{\partial^2 \mathbf{r}_{app,k}^*}{\partial x_k^2} < 0$  and  $\frac{\partial^2 \mathbf{r}_{app,k}^*}{\partial y_k^2} < 0$  because  $\frac{\partial \mathbf{r}_k^*}{\partial d_{i,k}} \Big|_{(d_{a,0,k}, d_{i,0,k})} < 0$  and  $\frac{\partial \mathbf{r}_k^*}{\partial d_{a,k}} \Big|_{(d_{a,0,k}, d_{i,0,k})} < 0$  are negative terms  $\forall d_{a,0,k} > 0, \forall d_{i,0,k} > 0$ . Furthermore, we have that  $\frac{\partial^2 \mathbf{r}_{app,k}^*}{\partial x_k^2} \frac{\partial^2 \mathbf{r}_{app,k}^*}{\partial y_k^2} - \left( \frac{\partial^2 \mathbf{r}_{app,k}^*}{\partial x_k \partial y_k} \right)^2 > 0$ . Therefore, the Hessian is negative definite and  $\mathbf{r}_{app,k}^*$  is a concave function of  $q_k = [x_k, y_k]$ .

## APPENDIX C

In this appendix, we prove that the sequence of solutions provided by *RMAP* converges to a KKT point of *P3* if, in each iteration  $j$ ,  $\bar{r}_{map,j} \geq r_{min}$ . We first observe that, when this condition holds, Lines 7-9 of *RMAP* does not affect the solution. Then, solving *P3* by *RMAP*, is equivalent to solving *P3* by using an SCO algorithm for which the convergence to a KKT point of *P3* follows from [42]. The convergence is guaranteed for every feasible initial solution and every trust region size  $T_k > 0$ . This proves the second part of Theorem 1.

## APPENDIX D

Now, we prove that *RMAP* converges even when condition  $\bar{r}_{map,j} \geq r_{min}$  does not hold for each iteration. More precisely, for each iteration  $n$  such that  $\bar{r}_{map,n} < r_{min}$ , *RMAP* sets  $\mathbf{q}_n = \mathbf{q}_{n-1}$  and decreases  $T_k$  for a certain timeslot  $k$ . Then, we can have one of the following three cases:

- *Case 1:*  $T_k > 0, \forall k$ . *RMAP* continues solving problem *P3* from iteration  $j = n + 1$  with  $\mathbf{q}_{n-1}$  as the initial feasible solution and  $T_k > 0, \forall k$ . As proved in Appendix C, if for the

successive iterations, i.e.,  $\forall j > n + 1$ , we have that  $\bar{r}_{map,j} \geq r_{min}$ , *RMAP* still converges to a KKT point of *P3*. Otherwise, for each iteration  $n$  such that  $\bar{r}_{map,n} < r_{min}$ , Lines 8 and 9 are repeated and this proof follows either *Case 1* or *Case 2* whether  $T_k > 0, \forall k$  or  $T_k = 0$  for a certain timeslot, respectively. If  $T_k = 0, \forall k$ , the proof follows *Case 3*.

- *Case 2*:  $T_k = 0$  for a certain timeslot  $k$  and iteration  $n$ . In this case, we have that constraint (23e) of *P4* becomes:

$$\|q_{j,k} - q_{j-1,k}\|_2 \leq T_k = 0, \forall j > n.$$

This is equivalent to adding the following affine constraints to *P3* and *P4*, respectively:

$$q_k = q_{k,n-1}, \text{ and } q_{k,j} = q_{k,n-1}.$$

The constraints, in fact, fix the position of the robot at a certain timeslot  $k$ . Given these constraints, we are free to set  $T_k > 0$ . Thus, from iteration  $j > n$ , *RMAP* solves a modified version of *P3* (*P3'*), starting from initial solution  $q_{n-1}$  and  $T_k > 0, \forall k$  by iteratively solving a modified version of *P4* (*P4'*). Note that adding this affine constraint to *P3* and *P4* does not change the convexity of the latter. As done in Appendix C, we can prove that *RMAP* converges to a KKT point of *P3'* if  $\forall j > n + 1$ , we have that  $\bar{r}_{map,j} \geq r_{min}$  holds. Otherwise, if  $\bar{r}_{map,j} < r_{min}$  for a certain iteration, the proof follows *Case 1* or *Case 2*, whether  $T_k > 0, \forall k$  or  $T_k = 0$  for a certain timeslot, respectively. If  $T_k = 0, \forall k$ , the proof follows *Case 3*.

- *Case 3*:  $T_k = 0, \forall k$ . In this case, the robot's position for each timeslot is fixed, and *RMAP* has converged to a solution.

Thus, we have that *RMAP* either converges to a KKT point of *P3* or to a KKT point of a modified problem where, for some or for all the timeslots, the robot's positions are fixed.

## REFERENCES

- [1] R. Sabella, A. Thuelig, M. C. Carrozza, and M. Ippolito, "Industrial automation enabled by robotics, machine intelligence and 5G," *Ericsson Technology Review*, 2018.
- [2] M. Giordani, M. Polese, M. Mezzavilla, S. Rangan, and M. Zorzi, "Toward 6G networks: Use cases and technologies," *IEEE Communications Magazine*, vol. 58, no. 3, pp. 55–61, 2020.
- [3] J. Wen, L. He, and F. Zhu, "Swarm robotics control and communications: Imminent challenges for next generation smart logistics," *IEEE Communications Magazine*, vol. 56, no. 7, pp. 102–107, 2018.
- [4] M. Cheffena, "Industrial wireless communications over the millimeter wave spectrum: opportunities and challenges," *IEEE Communications Magazine*, vol. 54, no. 9, pp. 66–72, Sep. 2016.



- [5] J. Engelmann, *Methoden und Werkzeuge zur Planung und Gestaltung energieeffizienter Fabriken*. IBF, 2009. [Online]. Available: <https://books.google.se/books?id=XWqSwAEACAAJ>
- [6] C. Tatino, N. Pappas, I. Malanchini, L. Ewe, and D. Yuan, "On the benefits of network-level cooperation in millimeter-wave communications," *IEEE Transactions on Wireless Communications*, vol. 18, no. 9, pp. 4408–4424, 2019.
- [7] W. Khawaja, O. Ozdemir, Y. Yapici, I. Guvenc, and Y. Kakishima, "Coverage enhancement for mm wave communications using passive reflectors," in *11th Global Symposium on Millimeter Waves (GSMM)*, 2018, pp. 1–6.
- [8] Q. Zhang, W. Saad, and M. Bennis, "Millimeter wave communications with an intelligent reflector: Performance optimization and distributional reinforcement learning," 2020. [Online]. Available: <https://arxiv.org/abs/2002.10572>
- [9] P. Wang, J. Fang, X. Yuan, Z. Chen, and H. Li, "Intelligent reflecting surface-assisted millimeter wave communications: Joint active and passive precoding design," *IEEE Transactions on Vehicular Technology*, pp. 1–1, 2020.
- [10] E. Basar, M. Di Renzo, J. De Rosny, M. Debbah, M. Alouini, and R. Zhang, "Wireless communications through reconfigurable intelligent surfaces," *IEEE Access*, vol. 7, pp. 116 753–116 773, 2019.
- [11] C. Liaskos, S. Nie, A. Tsioliaridou, A. Pitsillides, S. Ioannidis, and I. Akyildiz, "A new wireless communication paradigm through software-controlled metasurfaces," *IEEE Communications Magazine*, vol. 56, no. 9, pp. 162–169, 2018.
- [12] E. Björnson, O. Özdoğan, and E. G. Larsson, "Intelligent reflecting surface versus decode-and-forward: How large surfaces are needed to beat relaying?" *IEEE Wireless Communications Letters*, vol. 9, no. 2, pp. 244–248, 2020.
- [13] Yongguo Mei, Yung-Hsiang Lu, Y. C. Hu, and C. S. G. Lee, "Energy-efficient motion planning for mobile robots," in *IEEE International Conference on Robotics and Automation, Proceedings ICRA '04*, vol. 5, 2004, pp. 4344–4349 Vol.5.
- [14] S. Liu and D. Sun, "Minimizing energy consumption of wheeled mobile robots via optimal motion planning," *IEEE/ASME Transactions on Mechatronics*, vol. 19, no. 2, pp. 401–411, 2014.
- [15] Y. Zhao, Y. Wang, M. Zhou, and J. Wu, "Energy-optimal collision-free motion planning for multiaxis motion systems: An alternating quadratic programming approach," *IEEE Transactions on Automation Science and Engineering*, vol. 16, no. 1, pp. 327–338, 2019.
- [16] T. Setter and M. Egerstedt, "Energy-constrained coordination of multi-robot teams," *IEEE Transactions on Control Systems Technology*, vol. 25, no. 4, pp. 1257–1263, 2017.
- [17] Y. Yan and Y. Mostofi, "Co-optimization of communication and motion planning of a robotic operation under resource constraints and in fading environments," *IEEE Transactions on Wireless Communications*, vol. 12, no. 4, pp. 1562–1572, 2013.
- [18] U. Ali, H. Cai, Y. Mostofi, and Y. Wardi, "Motion-communication co-optimization with cooperative load transfer in mobile robotics: An optimal control perspective," *IEEE Transactions on Control of Network Systems*, vol. 6, no. 2, pp. 621–632, June 2019.
- [19] J. Scherer and B. Rinner, "Multi-robot persistent surveillance with connectivity constraints," *IEEE Access*, vol. 8, pp. 15 093–15 109, 2020.
- [20] G. A. Hollinger and S. Singh, "Multirobot coordination with periodic connectivity: Theory and experiments," *IEEE Transactions on Robotics*, vol. 28, no. 4, pp. 967–973, Aug. 2012.
- [21] E. F. Flushing, L. M. Gambardella, and G. A. Di Caro, "Simultaneous task allocation, data routing, and transmission scheduling in mobile multi-robot teams," in *IEEE/RSJ International Conference on Intelligent Robots and Systems (IROS)*, 2017, pp. 1861–1868.
- [22] J. Fink, A. Ribeiro, and V. Kumar, "Robust control of mobility and communications in autonomous robot teams," *IEEE Access*, vol. 1, pp. 290–309, 2013.
- [23] J. Stephan, J. Fink, V. Kumar, and A. Ribeiro, "Concurrent control of mobility and communication in multirobot systems," *IEEE Transactions on Robotics*, vol. 33, no. 5, pp. 1248–1254, 2017.

- [24] S. Gil, S. Kumar, D. Katabi, and D. Rus, "Adaptive communication in multi-robot systems using directionality of signal strength," *The International Journal of Robotics Research*, vol. 34, pp. 946 – 968, 2015.
- [25] J. Sachs, K. Wallstedt, F. Alriksson, and G. Eneroth, "Boosting smart manufacturing with 5G wireless connectivity," Ericsson Technology Review, 2019.
- [26] C. Pielli, T. Ropitault, and M. Zorzi, "The potential of mmwaves in smart industry: Manufacturing at 60 GHz," in *17th International Conference on Ad Hoc Networks and Wireless (AD HOC-NOW)*, 2018, pp. 64–76.
- [27] S. Saponara, F. Giannetti, B. Neri, and G. Anastasi, "Exploiting mm-wave communications to boost the performance of industrial wireless networks," *IEEE Transactions on Industrial Informatics*, vol. 13, no. 3, pp. 1460–1470, 2017.
- [28] Z. Xiao, P. Xia, and X. Xia, "Enabling UAV cellular with millimeter-wave communication: potentials and approaches," *IEEE Communications Magazine*, vol. 54, no. 5, pp. 66–73, 2016.
- [29] L. Zhang et al., "A survey on 5G millimeter wave communications for UAV-assisted wireless networks," *IEEE Access*, vol. 7, pp. 117 460–117 504, 2019.
- [30] C. Tatino, N. Pappas, and D. Yuan, "Multi-robot association-path planning in millimeter-wave industrial scenarios," *Accepted in IEEE Networking Letters*, 2020.
- [31] S. Zhang and R. Zhang, "Radio map based path planning for cellular-connected UAV," in *2019 IEEE Global Communications Conference (GLOBECOM)*, 2019, pp. 1–6.
- [32] Y. Zeng and R. Zhang, "Energy-efficient UAV communication with trajectory optimization," *IEEE Transactions on Wireless Communications*, vol. 16, no. 6, pp. 3747–3760, 2017.
- [33] A. Alsharoa, H. Ghazzai, M. Yuksel, A. Kadri, and A. E. Kamal, "Trajectory optimization for multiple UAVs acting as wireless relays," in *IEEE International Conference on Communications Workshops (ICC Workshops)*, 2018, pp. 1–6.
- [34] E. Fountoulakis, G. S. Paschos, and N. Pappas, "UAV trajectory optimization for time constrained applications," *IEEE Networking Letters*, vol. 2, no. 3, pp. 136–139, 2020.
- [35] M. Hua et al., "Power-efficient communication in UAV-aided wireless sensor networks," *IEEE Communications Letters*, vol. 22, no. 6, pp. 1264–1267, 2018.
- [36] Z. Zhou et al., "Energy-efficient industrial internet of UAVs for power line inspection in smart grid," *IEEE Transactions on Industrial Informatics*, vol. 14, no. 6, pp. 2705–2714, 2018.
- [37] D. Ma, M. Ding, and M. Hassan, "Enhancing cellular communications for UAVs via intelligent reflective surface," 2020. [Online]. Available: <https://arxiv.org/abs/1911.07631>
- [38] Q. Zhang, W. Saad, and M. Bennis, "Reflections in the sky: Millimeter wave communication with UAV-carried intelligent reflectors," 2019. [Online]. Available: <https://arxiv.org/abs/1908.03271>
- [39] L. Ge, P. Dong, H. Zhang, J. Wang, and X. You, "Joint beamforming and trajectory optimization for intelligent reflecting surfaces-assisted UAV communications," *IEEE Access*, vol. 8, pp. 78 702–78 712, 2020.
- [40] S. Li, B. Duo, X. Yuan, Y. Liang, and M. Di Renzo, "Reconfigurable intelligent surface assisted UAV communication: Joint trajectory design and passive beamforming," *IEEE Wireless Communications Letters*, vol. 9, no. 5, pp. 716–720, 2020.
- [41] X. Zhang, A. Liniger, and F. Borrelli, "Optimization-based collision avoidance," *IEEE Transactions on Control Systems Technology*, pp. 1–12, 2020.
- [42] B. R. Marks and G. P. Wright, "A general inner approximation algorithm for nonconvex mathematical programs," *Operations Research*, vol. 26, no. 4, pp. 681–683, 1978. [Online]. Available: <http://www.jstor.org/stable/169728>